

4 Magnetic Amplification of Photoevaporation: Coupled Dynamo and Ohmic Heating in Hot Saturns

5 KOEN SCHENCK¹ AND HOWARD CHEN^{1, 2}

6 ¹*Department of Aerospace, Physics, and Space Sciences, Florida Institute of Technology, Melbourne, FL 32901*

7 ²*Sellers Exoplanet Environments Collaboration (SEEC), NASA Goddard Space Flight Center, Greenbelt, MD 20771*

8 ABSTRACT

9 The coupled thermal and mass-loss evolution of close-in gaseous exoplanets is governed by a com-
10 bination of post-formation processes. For highly irradiated exoplanets ($T_{\text{eq}} > 1000$ K), hydrodynamic
11 escape during the high-EUV phases of stellar evolution and Ohmic dissipation from the interaction
12 between ionized winds and planetary magnetic fields both play central roles in shaping their long-term
13 outcomes. Here, we compute time-dependent planetary magnetic fields from convective dynamo scal-
14 ing and use them to self-consistently evaluate volumetric Ohmic heating in the deep interiors of hot
15 Saturn-mass worlds. Our calculations span a range of planetary masses, core fractions, and orbital
16 separations, showing that magnetic dissipation can substantially inflate radii and enhance mass-loss
17 rates, especially in systems with large core-to-envelope ratios. These effects establish a coupled path-
18 way of thermal inflation and erosion that naturally drives low-mass hot Saturns toward instability
19 and strong enhancement in the loss of their H/He envelopes. The results suggest that magnetically
20 induced heating is a key regulator of the close-in exoplanet population and may underlie the origin of
21 the hot-Saturn desert.

22 1. INTRODUCTION

23 The physical diversity of close-in exoplanets reflects the competing effects of interior heat sources, stellar irradiation,
24 and atmospheric escape. A planet's thermal evolution depends on how these energy reservoirs exchange and dissipate
25 over time, regulating its radius, luminosity, and volatile retention. Tidal dissipation in eccentric orbits (Jackson et al.
26 2008; Ginzburg & Sari 2016) and misaligned orbits (Sethi & Millholland 2025) can inject substantial power into the
27 deep interior, delaying thermal contraction on gaseous planets. Long-lived radiogenic decay and residual accretional
28 heat likewise maintain intrinsic luminosity over gigayear timescales (Hubbard et al. 2002). In contrast, high-energy
29 stellar radiation in the X-ray and extreme-ultraviolet (XUV; 10–1200 Å) range impart energy in the upper atmosphere
30 and can drive hydrodynamic escape of light gases (Lopez & Fortney 2013; Owen & Wu 2017; Gu & Chen 2023),
31 removing substantial fractions of a planet's envelope and shaping the observed “radius valley.”

32 Ohmic dissipation has emerged as a particularly compelling mechanism to explain the anomalously large radii of
33 many close-in gas giants (“hot Jupiters”). In their seminal work, Batygin & Stevenson (2010) demonstrated that strong
34 stellar irradiation drives ionized winds in a hot Jupiter's atmosphere, which, interacting with an imposed planetary
35 magnetic field, induce currents that penetrate and heat the deep interior. Follow-up studies have mapped out how
36 wind speed, conductivity profiles, and rotation modulate Ohmic power (Perna et al. 2010; Rauscher & Menou 2013;
37 Wu & Lithwick 2013; Cohen et al. 2024) and have demonstrated correlations between incident flux and radius inflation
38 across gas-giant populations (Ginzburg & Sari 2016; Thorngren & Fortney 2018). Others even suggest that Ohmic
39 heating may play a role down to sub-Neptune masses, providing a continuous heating mechanism as planets transition
40 from gas giants to smaller envelopes (Pu & Valencia 2017). More recently, Viganò et al. (2025) used Ohmically-heated
41 evolutionary calculations to estimate the envelope wind intensities in order to reproduce the range of observed radii.

42 Planetary magnetic fields are central to the Ohmic paradigm, yet their strengths and geometries remain poorly
43 constrained, especially for lower-mass objects. In the Solar System, Jupiter's dipole moment is roughly 10^5 times
44 Earth's, while Saturn, Uranus, and Neptune exhibit weaker, more complex fields (Connerney et al. 2018). For exo-
45 planets, dynamo-scaling laws tied to convective heat flux predict field strengths of order 1–100 G across gas giants

Table 1: Planetary Parameter Space and Key Model Assumptions

Quantity	Symbol	Values / Range	Units	Notes
Planet Mass	M_p	60, 80, 100	M_\oplus	Core + envelope included
Orbital Separation	a	0.02, 0.04, 0.05	AU	Circular orbits assumed
Initial Envelope Fraction	f_{env}	0.7, 0.8, 0.9	–	Fraction of M_p in H/He envelope
Stellar Age	t_\star	$10^{6.5} \text{--} 10^9$	yr	Sampled logarithmically
Ohmic Heating	–	On / Off	–	Applied following standard scaling prescription (core)
Magnetic Field Strength	B_{dip}	80–100	G	Surface dipole; consistent with convective dynamo scaling
Mass Loss Rate	\dot{M}	Computed	M_\odot/yr	Energy-limited atmospheric escape
Planet Radius	R_p	Computed	R_\odot	Converted to R_J where relevant
Equation of State	–	H/He EOS	–	Standard MESA implementation
Convective Shell Mass	Δm_{conv}	Computed	M_\oplus	Depth of active dynamo region (varies with age and irradiation)
Conducting Shell Volume	V_{shell}	Computed	cm^3	Region over which Ohmic dissipation is integrated
Magnetic Field Scaling	–	$B \propto (F_{\text{conv}}\rho)^{1/3}$	–	Field linked to internal convective power

and sub-Neptunes (Christensen et al. 2009; Reiners & Christensen 2010). Observational searches for radio emission or bow-shock signatures offer tantalizing but inconclusive hints (Vidotto et al. 2010; Hess & Zarka 2011).

Previous Ohmic-heating studies have typically prescribed planetary magnetic fields as fixed inputs rather than evolving them consistently with the planet’s thermal and structural evolution. In reality, the field strength is set by convective luminosity and interior temperature gradients, quantities that Ohmic dissipation itself modifies, implying a time-dependent feedback between magnetic activity and energy deposition. This coupling is especially relevant for sub-Saturn and sub-Neptune planets, whose modest envelopes and diverse cooling histories can drive a wide range of dynamo behaviors. Here we incorporate a dynamo-scaling prescription directly into the Ohmic-heating framework, enabling more realistic predictions of radius inflation, magnetic observables, and long-term thermal evolution in the growing sample of hot Saturn-mass exoplanets. Here we calculate the interior Ohmic dissipation with an evolving dynamo in the hot-Saturn mass range, which is distinct from previous upper-atmosphere induction studies.

2. CALCULATIONS & NUMERICAL MODEL

In this study, we employed the stellar and planetary evolution code MESA (Modules for Experiments in Stellar Astrophysics; Paxton et al. 2010, 2013, 2015) to model the thermal evolution of exoplanets in the sub-Saturn mass range (approximately 60–100 M_\oplus). The MESA-planets suite 12778 version we used is based on previous work of Chen & Rogers (2016), Malsky & Rogers (2020), and Gu & Chen (2023). However, we turned off diffusive escape in our calculations here. Our models focused specifically on planets with hydrogen–helium (H/He) envelopes comprising between 1% and 10% of the total planetary mass. Equilibrium temperatures were chosen between 1300 K and 1500 K, motivated by previous findings that ohmic dissipation is most efficient within this temperature window; higher equilibrium temperatures typically result in negligible radius inflation for planets above Saturn mass, whereas lower temperatures significantly reduce heating efficiency (e.g., Batygin & Stevenson 2010; Pu & Valencia 2017).

Each planetary model is characterized by three primary parameters: planetary mass (fixed within each simulation), orbital separation, and envelope mass fraction (H/He ratio). Parameter ranges were guided by earlier modeling studies (Stevenson 1983; Kilmetis et al. 2024; Pu & Valencia 2017). Table 1 summarizes the range of planetary parameter space explored. The structural configuration in our MESA planet models consists of a well-defined core (either rocky or diffuse depending on the scenario considered) and an overlying gaseous envelope primarily composed of H and He, following standard assumptions employed widely in the literature.

2.1. *Interiors and Dynamo Criterion*

We estimate the magnetic field strength generated within the dynamo region using the convective power scaling commonly adopted in planetary dynamo studies (e.g., Christensen et al. (2009)). In this framework, the rms dynamo field B_{dyn} is proportional to the cube root of the convective power available to drive the dynamo and depends weakly on the local density. The scaling can be written as

$$B_{\text{dyn}} \propto (\mu_0 \rho_{\text{ref}})^{1/2} \left(\frac{F_{\text{conv,ref}}}{\rho_{\text{ref}}} \right)^{1/3}, \quad (1)$$

where μ_0 is the magnetic permeability of free space, ρ_{ref} is the reference density within the dynamo region, and $F_{\text{conv,ref}}$ is the convective heat flux evaluated at the base of that region. This formulation implicitly accounts for the volume-integrated convective power within the dynamo shell. A dimensionless prefactor of order unity and an efficiency factor f_{ohm} (representing the fraction of convective power converted into magnetic energy) are typically included to account for dynamical and ohmic conversion efficiencies calibrated from numerical dynamo simulations.

The field strength at the planetary surface can then be estimated by assuming a dipolar decay of the field from the dynamo radius R_{dyn} to the surface R_p :

$$B_{\text{dip}} \approx B_{\text{dyn}} \left(\frac{R_{\text{dyn}}}{R_p} \right)^3. \quad (2)$$

The convective heat flux used in this relation governs both energy transport and dynamo vigor. The value is obtained from the internal structure model or from mixing-length theory, and can be expressed as

$$F_{\text{conv}} = \frac{2(C_p(z))T(z)\rho(z)^2 v_{\text{conv}}(z)^3}{-P(z) \left(\frac{d \ln \rho}{d \ln T} \Big| P_{\text{gas}} \right)}, \quad (3)$$

where c_p is the specific heat at constant pressure ($\text{J kg}^{-1} \text{K}^{-1}$), obtained from the equation of state; T is the local temperature; $v_{\text{conv}}(z)$ is the mixing-length convective velocity (m s^{-1}), computed by **MESA**; Δ_s represents the superadiabatic entropy excess; and

$$\left(\frac{d \ln \rho}{d \ln T} \right)_{P_{\text{gas}}}$$

is the thermodynamic partial derivative from the equation of state, evaluated at constant gas pressure. In practice, $F_{\text{conv,ref}}$ is defined as the value of the convective flux at the base of the dynamo region, providing the most direct measure of the power available to sustain the magnetic field. This approach relates the dynamo field strength to the internal convective properties of the planet in a manner consistent with results from numerical simulations and empirical scalings for both solar-system and exoplanetary dynamos.

The convective regions previously defined by Christensen et al. (2009). suggest that larger Jovian exoplanets' convective regions are not applicable to Saturn's. In the absence of a better convective profile, we utilize the dynamo scaling laws outlined below.

The dynamo region is defined by the magnetic Reynolds number, which is calculated as

$$\text{Re}_{\text{mag}} = v_{\text{conv}}(z) (R_{\text{start}} - R_{\text{end}}) \frac{T(z)^{3/2}}{4\pi}, \quad (4)$$

where $v_{\text{conv}}(z)$ is the convective velocity evaluated between the inner core boundary (R_{start}) and the outer convective limit (R_{end}), and $T(z)$ is the local temperature. We concretely define the onset of a dynamo regime when the magnetic Reynolds number exceeds the critical threshold $\text{Re}_{\text{mag,crit}} = 50$, following the methodology of Kilmetis et al. (2024) and Christensen et al. (2009). We note, however, that this value is arbitrary.

The use of the Reynolds number as a dynamo criterion in this study arises from the quantities readily available within **MESA**. The convective velocity, $v_{\text{conv}}(z)$, is computed from the standard mixing-length formulation used to evaluate convective flux and velocity in **MESA**, as defined in Equation (3). In the absence of a detailed electrical conductivity profile, we used the convective flux to propagate through the magnetic Reynolds number calculation. As a result, the dipole magnetic field strengths (B_{dip}) evolved in each simulation suggest that dynamo regions form early in the planet's thermal evolution, thereby supporting the validity of using the critical Reynolds number criterion.

2.2. Ohmic Dissipation

In the context of radius inflation, Ohmic dissipation acts as an additional internal heat source that counteracts radiative cooling and delays planetary contraction. The efficiency of this process depends on both the conductivity profile and the equilibrium temperature T_{eq} . Previous studies (e.g., Batygin & Stevenson 2010; Thorngren & Fortney 2018) have shown that Ohmic heating is most effective in atmospheres with $T_{\text{eq}} \sim 1500\text{--}1600$ K, where partial ionization enhances conductivity. However, the total heating rate Q_{heat} tends to increase monotonically with T_{eq} , consistent with the observed correlation between inflated radii and stellar irradiation for $T_{\text{eq}} \gtrsim 1000$ K. What decreases at higher

temperatures is not the absolute heating, but rather the *efficiency*

$$\epsilon_{\text{Ohm}} = \frac{Q_{\text{heat}}}{L_{\text{irr}}},$$

as the stellar irradiance rises more rapidly than the additional Ohmic power.

In this study, our implementation focuses on the coupling between the magnetic field, conductivity, and convective flow without explicitly prescribing a temperature-dependent efficiency function. However, our models reproduce the qualitative trend that stronger irradiation (and hence higher atmospheric temperatures) enhances Ohmic dissipation, while planets with larger masses—having deeper gravitational wells—exhibit smaller fractional radius responses to a given Q_{ohm} , (see also [Viganò et al. 2025](#)).

We calculate Ohmic dissipation from zonal flows interacting with the planetary magnetic field using the local expression

$$P_{\text{Ohm}} = \int_{V_{\text{shell}}} \sigma(r, \theta) |\mathbf{v}(r, \theta) \times \mathbf{B}(r, \theta)|^2 dV, \quad (5)$$

where the integration is carried out over the conducting shell defined between r_{start} and r_{end} (add citation). Here, $\sigma(r, \theta)$ is the electrical conductivity (S m^{-1}), \mathbf{v} the zonal flow (m s^{-1}), and \mathbf{B} the magnetic field (G).

In practice, we (evaluate) a volume-averaged form,

$$P_{\text{Ohm}} \approx \langle \sigma \rangle \langle v_{\text{wind}}^2 \rangle \langle B^2 \rangle V_{\text{shell}} f_{\text{geom}}, \quad (6)$$

where $\langle \cdot \rangle$ denotes a suitable spatial average and f_{geom} accounts for local angular factors of order unity. The Ohmic heating rate per unit mass of the convective shell is then

$$q_{\text{Ohm}} = \frac{P_{\text{Ohm}}}{\Delta m_{\text{conv}}}. \quad (7)$$

We compute $\sigma(r, T, P)$ using the ionization and pressure-ionization equation of state prescriptions implemented in MESA, and depends primarily on local tempertaure and density. We adopt a normalized zonal wind speeds v_{wind} , following non-dimensional ohmic heating studies [Christensen et al. \(2009\)](#). In this formulation, v_{wind} acts as a scaling parameter that sets the strength of the interaction between atmospheric flows and the magnetic field, rather than representing a physical velocity in m s^{-1} . This convention isolates the dependence of Ohmic dissipation on the magnetic and conductive structure of the envelope, while avoiding additional uncertainties associated with atmospheric circulation modeling. The sensitivity to wind speed can be recovered a posteriori by rescaling $q_{\text{Ohm}} \propto v_{\text{wind}}^2$ over the desired dynamical range.

Finally, the volumetric Ohmic heating rate is computed as

$$\dot{Q}_{\text{ohm}} = \frac{B_{\text{dip}}(T)^2 v_{\text{wind}}^2 V_{\text{shell}}}{\Delta m_{\text{conv}}}, \quad (8)$$

where Q_{ohm} here is the integrated form of the previous averaged q_{ohm} value Eq. 7 in units of W/kg . Here is an expanded view of the 1D structural energy equation:

$$\frac{dr_d L}{dr} = 4\pi r^2 \rho(r) [q_{\text{ohm}}(r) + q_{\text{radio}}(r) - T(r) \dot{s}(r)], \quad (9)$$

where $q_{\text{ohm}}(r)$ has units of W kg^{-1} (specific Ohmic heating), $q_{\text{radio}}(r)$ has units of W kg^{-1} (specific radiogenic heating), $\dot{s} \equiv \frac{ds}{dt}$ is the Lagrangian specific-entropy change with units of $\text{J kg}^{-1} \text{K}^{-1} \text{s}^{-1}$, and $T \dot{s}$ therefore has units of W kg^{-1} .

v_{wind} is the characteristic zonal wind speed, V_{shell} the volume of the conducting region, starting at the previously defined R_{start} , and Δm_{conv} the mass of the convective shell. This formulation self-consistently couples the magnetic field strength, convective flux, and Ohmic power, allowing the model to evolve the planetary interior, radius, and mass-loss rate in tandem.

147 2.3. *Radiative-Recombination-, Energy-Limited Escape, & Core Heat*

148 In strongly irradiated regimes, the atmospheric escape flow becomes hydrodynamic, driven by the combined stellar
 149 X-ray and EUV flux (F_{XUV}) that deposits energy above the homopause and accelerates the upper atmosphere to
 150 transonic velocities (near the local sound speed; Tian et al. 2005; Murray-Clay et al. 2009). The XUV band spans
 151 approximately 1–912 Å, encompassing both the soft X-ray (1–100 Å) and extreme ultraviolet (100–912 Å) domains
 152 most effective at heating and ionizing the upper atmosphere. The absorbed high-energy flux sets the available power
 153 for escape, such that the energy-limited rate naturally scales with F_{XUV} rather than the bolometric stellar flux. This
 154 coupling captures the transition between weak, photon-limited escape and full hydrodynamic outflow.

155 Wind temperature: The outflow rapidly reaches a nearly isothermal temperature set by a balance between photoioniza-
 156 tion heating and Ly α cooling. We adopt

$$T_{\text{wind}} = 10^4 \text{ K}, \quad (10)$$

157 consistent with 1D hydrodynamic simulations (Murray-Clay et al. 2009; Owen & Wu 2013). Tests with $T_{\text{wind}} = (8-$
 158 $12) \times 10^3 \text{ K}$ modify M_{RR} by less than 30%.

159 Radiative Recombination Coefficient: The hydrogen recombination coefficient varies weakly with temperature as

$$\alpha_{\text{rec}} \approx 2.7 \times 10^{-13} \left(\frac{T}{10^4 \text{ K}} \right)^{-0.7} \text{ cm}^3 \text{ s}^{-1}, \quad (11)$$

160 following Storey & Hummer (1995). This scaling is applied self-consistently when evaluating Equation (9) at each
 161 timestep.

162 Tidal Correction: The tidal enhancement factor K_{tidal} depends on the ratio of the EUV absorption radius to the
 163 Roche-lobe radius, both of which evolve as the planet loses mass. At each timestep we update K_{tidal} using the
 164 instantaneous M_p and R_{EUV} values.

165 Here, atmospheric escape is incorporated through the standard energy-limited prescription (Watson et al. 1981;
 166 Lammer et al. 2003; Owen & Wu 2013), with the mass-loss rate.

$$\dot{M}_{\text{env}} = -\frac{\varepsilon_{\text{EUV}} \pi F_{\text{EUV}} R_p R_{\text{EUV}}^2}{GM_p K_{\text{tidal}}}, \quad (12)$$

167 where $\varepsilon_{\text{EUV}} = 0.1$ denotes the heating efficiency, K_{tidal} accounts for Roche-lobe effects, and R_{EUV} is the EUV absorp-
 168 tion radius estimated from the photospheric scale height.

169 At high EUV fluxes ($F_{\text{EUV}} \gtrsim 10^4 \text{ erg s}^{-1} \text{ cm}^{-2}$), the flow enters the radiation-recombination limited regime where
 170 photoionizations are balanced by radiative recombinations and Ly α cooling fixes the wind temperature near $T_{\text{wind}} \sim$
 171 10^4 K . In this regime, the energy-limited assumption breaks down and the mass-loss rate follows the expression of
 172 Murray-Clay et al. (2009):

$$\dot{M}_{\text{rr}} = -\pi \left(\frac{GM_p}{c_s^2} \right)^2 c_s m_H \left(\frac{F_{\text{EUV}} GM_p}{h\nu_0 \alpha_{\text{rec}} R_{\text{EUV}}^2 c_s^2} \right)^{1/2} \exp \left[2 - \frac{GM_p}{c_s^2 R_{\text{EUV}}} \right], \quad (13)$$

173 where \dot{M}_{RR} is the radiative-recombination-limited mass-loss rate, G is the gravitational constant, and M_p is the
 174 planetary mass. The quantity $c_s = (2k_B T_{\text{wind}} / m_H)^{1/2}$ is the isothermal sound speed in the wind, with k_B the Boltzmann
 175 constant, T_{wind} the adopted wind temperature, and m_H the mass of a hydrogen atom. The parameter F_{EUV} is the stellar
 176 EUV flux incident at the planet, $h\nu_0$ is a representative photon energy in the EUV band, $\alpha_{\text{rec}} \approx 2.7 \times 10^{-13} \text{ cm}^3 \text{ s}^{-1}$ is
 177 the hydrogen radiative recombination coefficient at 10^4 K , and R_{EUV} is the characteristic radius at which the bulk of
 178 the EUV photons are absorbed and where the flow is launched. This expression describes the radiative-recombination-
 179 limited regime, in which the flow structure is set by the balance between photoionization and radiative recombination
 180 (radiative equilibrium) rather than by a global energy-conservation constraint, and the mass-loss rate is therefore
 181 controlled by the rate at which ionizing photons can be converted into escaping ions.

182 Combined Mass-Loss Prescription: At each timestep, we compute both the energy-limited (\dot{M}_{EL}) and radia-
 183 tion-recombination-limited (\dot{M}_{RR}) mass-loss rates, and adopt

$$\dot{M} = \min(\dot{M}_{\text{EL}}, \dot{M}_{\text{RR}}) \quad (14)$$

184 to ensure a smooth, continuous transition between the two escape regimes.

185 The planetary core luminosity,

$$L_{\text{core}} = -c_v M_{\text{core}} \frac{dT_{\text{core}}}{dt} + L_{\text{radio}}, \quad (15)$$

186 is added as an internal energy source using composition-dependent specific heats and radionuclide decay terms (Guillot
187 2010; Schubert et al. 1980).

188 2.4. Equation of State, Microphysics, and Interior Structure

189 We adopted a simplified time-evolving prescription for the stellar EUV luminosity based on a broken power-law
190 consistent with observational studies of low-mass stars (Ribas et al. (2005); Claire et al. (2012)).

191 During the early EUV-saturated phase (up to ~ 100 Myr), the EUV luminosity L_{euv} is held constant at a high level,
192 corresponding to 10^{-3} of the bolometric luminosity.

193 After this phase, L_{euv} decays as a power law in time, typically following $L_{\text{euv}} \propto t^{-1.23}$, following the parameterization
194 in Ribas et al. (2005) and also adopted in similar exoplanet atmospheric escape studies (Lopez & Fortney (2013);
195 Chen & Rogers (2016)). We evolve a spherically symmetric H/He envelope atop a heavy-element core using the
196 Saumon–Chabrier–van Horn EOS (SCvH) for H/He, with fixed bulk composition ($Y = 0.25$, $Z = 0.03$ unless stated),
197 and Rosseland-mean opacity tables from Freedman et al. (2014). The models employ a semi-grey atmospheric boundary
198 condition based on the $T(\tau)$ relation of Guillot (2010), allowing the photospheric pressure to vary dynamically with
199 optical depth rather than being fixed at a constant value. Radiative-convective transitions, irradiation, and envelope
200 cooling are evolved self-consistently using MESA’s `relax_irradiation` option, with initial conditions defined through
201 a reinflation procedure that restores the target interior entropy prior to time integration. Core heating is included via
202 a composition-dependent luminosity L_{core} (radioactive decay + thermal inertia) injected at the base of the envelope;
203 the envelope may also receive distributed heating from Ohmic dissipation as described below.

204 The interior follows the standard 1-D structure system:

$$\frac{dm}{dr} = 4\pi r^2 \rho, \quad (16)$$

$$\frac{dP}{dr} = -\frac{Gm\rho}{r^2}, \quad (17)$$

$$\frac{dL}{dr} = 4\pi r^2 \rho \left(q_{\text{ohm}} + q_{\text{radio}} - T \frac{ds}{dt} \right), \quad (18)$$

$$\frac{dT}{dr} = \frac{T}{P} \nabla \frac{dP}{dr}, \quad \nabla = \min(\nabla_{\text{rad}}, \nabla_{\text{ad}}), \quad (19)$$

205 where $\rho(P, T)$ is supplied by the EOS, q_{ohm} is the volumetric Ohmic heating rate (zero in non-Ohmic runs), and q_{radio}
206 captures any distributed radiogenic heating if present. The radiative temperature gradient is

$$\nabla_{\text{rad}} = \frac{3\kappa LP}{64\pi\sigma GmT^4}, \quad (20)$$

207 with opacity $\kappa(P, T)$ from the tables, and σ the Stefan–Boltzmann constant; in convective zones we adopt the MESA
208 default mixing-length treatment, so that $\nabla = \nabla_{\text{ad}}$ where convection is efficient. Boundary conditions are set at the
209 photosphere via the $T(\tau)$ relation and at the inner edge by the specified L_{core} and core radius.

210 *Coupling to magnetic/Ohmic heating.*—The Ohmic source term q_{ohm} in Eq. (18) is supplied by our dynamo-linked
211 prescription: a convective-flux-based field B_{dyn} is mapped to the surface dipole B_{field} and converted to volumetric
212 heating \dot{Q}_{ohm} within the conducting shell; numerically, $q_{\text{ohm}} \equiv \dot{Q}_{\text{ohm}}/(4\pi r^2 \rho)$ and is added to MESA’s energy equation
213 while the structure iterates to equilibrium.

214 Additioanlly, In order to consistently assess mass loss within each planetary model, we adopt a spherically symmetric
215 continuity prescription and explicitly account for mass loss at the outer boundary. The local mass coordinate is defined
216 by

$$\frac{dm}{dr} = 4\pi r^2 \rho(r, t), \quad (21)$$

217 which is used to compute the instantaneous hydrostatic structure at each timestep. The total planetary mass evolves

218 due to atmospheric escape as

$$\frac{dM_p}{dt} = -\dot{M}_{\text{loss}}(t), \quad (22)$$

219 where \dot{M}_{loss} is obtained from the atmospheric escape prescription described in Section 2.2. Numerically, at each
220 timestep Δt , we remove a mass

$$\Delta M = \dot{M}_{\text{loss}} \Delta t \quad (23)$$

221 from the outermost shell(s) and remap the structure, conserving mass and internal energy before solving for the next
222 hydrostatic equilibrium. This quasi-static treatment is valid provided the wind speed in the interior remains small
223 compared with the local sound speed. If the wind penetrates deeply such that advective terms become non-negligible,
224 the full time-dependent continuity and momentum equations must be solved (Murray-Clay et al. 2009).

225 3. RESULTS

226 Figure 1 presents the temporal evolution of hydrodynamic mass-loss rates for planets of 60 and 80, M_{\oplus} subject to
227 varying orbital separations and envelope mass fractions. In both mass regimes, escape rates peak at $\dot{M}_{\text{env}} \sim 10^{12}$ –
228 $10^{13}, M_{\odot}, \text{yr}^{-1}$ during the early EUV-saturated phase of stellar evolution, followed by a monotonic decline as the
229 planets cool and contract. For the 60, M_{\oplus} models (Fig. 1a), closer orbital distances and more massive envelopes
230 sustain enhanced escape over extended intervals, whereas tenuous envelopes rapidly approach asymptotically low loss
231 rates. The 80, M_{\oplus} models (Fig. 1b) exhibit a similar decrease, though the sensitivity to envelope fraction is reduced
232 as the mass-loss rates converge by $\sim 10^8, \text{yr}$. These results demonstrate that both total mass and envelope fraction,
233 through their influence on the magnetic field strengths and the power of Ohmic heating, modulate the early and
234 long-term atmospheric escape.

235 We validate the dynamo regions via a non-ohmic heating diagnostic, in which we retrieve consistent magnetic dipole
236 values for the respective Saturn mass simulations in Table 2.

237 For the 100, M_{\oplus} cases (Fig. 1c), the overall trend is similar to the lower-mass models: mass-loss rates peak early, near
238 10^{12} – $10^{13}, M_{\odot}, \text{yr}^{-1}$, and then decline as the planets contract and the stellar EUV flux decreases. However, the higher
239 planetary mass stabilizes the envelope, producing faster convergence across different initial envelope fractions, and
240 by late times the mass-loss rates are nearly indistinguishable. Panel (d) highlights the impact of Ohmic dissipation
241 on radius evolution: planets with Ohmic heating remain more inflated than their non-Ohmic counterparts, with
242 differences of several tenths of a Jupiter radius persisting well into Gyr timescales. This sustained inflation, despite
243 ongoing mass loss, underscores the role of magnetically induced heating as a counteracting process to standard cooling
244 and contraction, particularly for planets with large initial H/He envelopes. Selected results are also summarized in
245 Table 3.

Table 2: Planetary radius and dipole magnetic field strength for varying orbital separation.

Sep (AU)	Planet Radius (R_{\oplus})	B_{dip} (G)
80 M_{\oplus}		
0.05	7.6082	98.5
0.04	7.6410	97.9
0.02	7.5082	94.6

246 Figure 2 shows the mass-loss rates for 60–100 M_{\oplus} planets at orbital separations of 0.02–0.05 AU, comparing sim-
247 ulations with and without Ohmic heating. In all cases, the non-Ohmic models (dashed curves) follow the expected
248 monotonic decline in escape rate as the envelopes cool and contract, tracing a nearly linear relationship between radius
249 and mass-loss rate. The inclusion of Ohmic dissipation (solid curves) produces a pronounced departure from this trend:
250 magnetic energy deposited in the deep interior inflates planetary radii and elevates atmospheric escape by roughly one
251 to two orders of magnitude. This amplification is most prominent for the 60 M_{\oplus} cases, where sustained Ohmic power
252 maintains inflated radii long after the stellar EUV flux declines, but remains evident across the entire Saturn-mass
253 regime.

254 These results demonstrate that Ohmic heating introduces a feedback loop between magnetic dissipation, thermal
255 expansion, and hydrodynamic escape. As the envelope inflates, the enhanced wind–field coupling strengthens interior

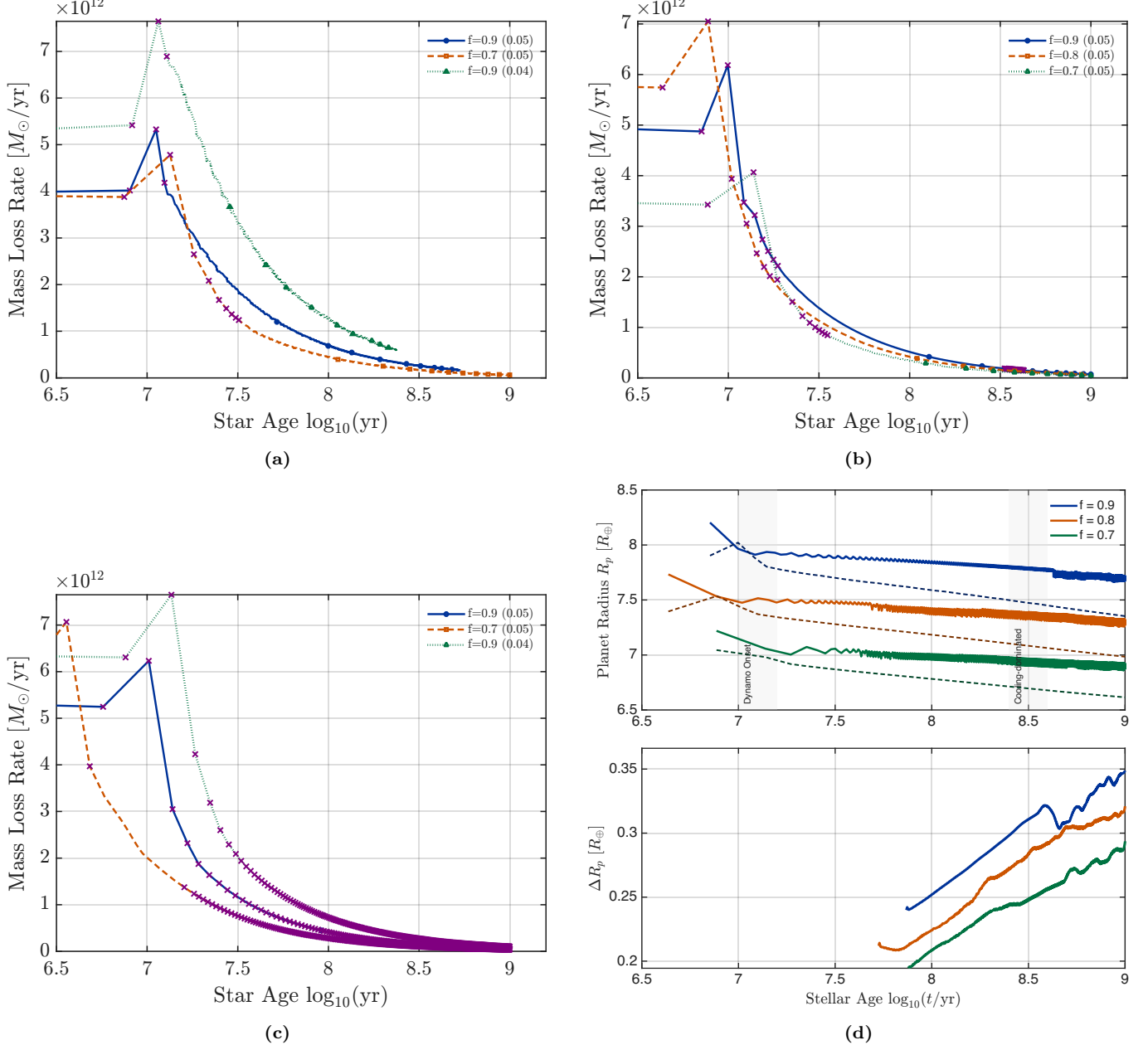


Figure 1: Coupled evolution of radius inflation and atmospheric escape for 60 , 80 , and $100 M_{\oplus}$ hot-Saturn models at orbital separations of 0.05 AU (a), 0.04 AU (b), and 0.02 AU (c), while panel (d) shows radius evolution with and without Ohmic heating. Solid curves denote simulations including Ohmic heating, while dashed curves show non-Ohmic counterparts. In all cases, magnetic dissipation drives larger radii and correspondingly higher mass-loss rates, enhancing escape by $\approx 1^{\circ}2$ dex relative to cooling-only models. The strongest amplification occurs for the $60 M_{\oplus}$ cases, where persistent Ohmic power sustains inflated radii even after the stellar EUV flux declines. Higher-mass planets show more modest divergence as deeper gravitational wells suppress runaway inflation. The departure from the near-linear radius–loss trend of the non-Ohmic models illustrates the self-reinforcing feedback between dynamo-driven heating, interior expansion, and hydrodynamic escape across the hot-Saturn regime.

currents, reinforcing both radius inflation and mass loss over Gyr timescales. The persistence of large radii despite significant atmospheric depletion is consistent with the exponential inflation mechanism proposed by Pu & Valencia (2017), highlighting the role of magnetic heating as a long-lived regulator of the evolution of hot exoplanets.

Table 3: Ohmic heating, mass-loss rate, and magnetic field for varying orbital separations of 80 and 60 M_{\oplus} planets.

Sep (AU)	Age (log[Gyr])	P_{ohm} (W)	\dot{M} (M_{\odot} yr $^{-1}$)	B (G)
80 M_{\oplus}				
0.05	6.8	5.46×10^{17}	1.12×10^{13}	9.50×10^1
0.05	7.0	4.25×10^{17}	3.46×10^{12}	1.02×10^2
0.05	8.0	2.73×10^{17}	5.13×10^{11}	1.02×10^2
0.04	6.7	6.79×10^{17}	1.65×10^{13}	9.43×10^1
0.04	7.0	3.47×10^{17}	6.78×10^{12}	1.03×10^2
0.04	8.0	3.35×10^{17}	9.03×10^{11}	1.00×10^2
0.02	6.0	6.61×10^{17}	4.11×10^{13}	9.79×10^1
0.02	7.0	6.62×10^{17}	1.45×10^{13}	9.74×10^1
0.02	8.0	3.33×10^{17}	5.29×10^{12}	9.55×10^1
60 M_{\oplus}				
0.05	6.9	5.30×10^{17}	7.31×10^{12}	8.69×10^1
0.05	7.0	3.79×10^{17}	4.75×10^{12}	9.48×10^1
0.05	8.0	2.40×10^{17}	6.94×10^{11}	9.38×10^1
0.04	6.9	6.60×10^{17}	8.89×10^{12}	8.64×10^1
0.04	7.0	4.61×10^{17}	7.37×10^{12}	9.35×10^1
0.04	8.0	2.98×10^{17}	1.27×10^{12}	9.26×10^1
0.02	6.0	5.82×10^{17}	4.88×10^{13}	9.12×10^1
0.02	7.0	5.89×10^{17}	1.69×10^{13}	9.12×10^1
0.02	8.0	5.89×10^{17}	8.02×10^{12}	8.99×10^1

The final outcomes of our models, summarized in Figure 2, reveal a non-linear dependence of magnetic field strength¹, Ohmic heating efficiency, and late-time mass-loss rates on orbital separation across the 60–100 M_{\oplus} regime. Panel (a) shows that magnetic dipole strengths generally increase with decreasing orbital distance, but with a pronounced maximum near 0.04 AU for the 60 M_{\oplus} case. This peak reflects the balance between vigorous convective fluxes, which favor dynamo activity, and the onset of rapid mass loss, which subsequently depletes the envelope and damps the dynamo. Because faster cooling enhances the intrinsic luminosity, lower-mass planets initially sustain stronger convective fluxes and thus stronger magnetic fields. Higher-mass planets, by contrast, cool more slowly and exhibit more muted variations, converging toward ~ 90 –100 G fields that are relatively insensitive to separation. Similarly, the Ohmic heating power in panel (b) rises sharply for close-in, lower-mass planets, reaching $\gtrsim 10^{18}$ W at 0.04 AU for the 60 M_{\oplus} models, while the 100 M_{\oplus} cases remain an order of magnitude lower.

The mass-loss rates (Fig. 1) show the enhanced susceptibility of lower-mass planets to total erosion. At $a = 0.02$ AU, the 60, M_{\oplus} models sustain $\dot{M}_{\text{env}} \sim 10^{13}, M_{\odot}, \text{yr}^{-1}$, whereas the 80 and 100, M_{\odot} cases decline to $\sim 10^{12}, M_{\odot}, \text{yr}^{-1}$. Beyond ~ 0.04 AU, all models exhibit sharply attenuated escape consistent with the radial decay of stellar EUV irradiation. The results indicate that Ohmic dissipation and dynamo-driven heating jointly destabilize the envelopes of close-in, low-mass hot Saturns, while more massive analogs remain thermally buffered against runaway inflation and escape. The coupling between magnetic energy deposition, envelope expansion, and hydrodynamic outflow is therefore expected to peak in the sub-Saturn regime, producing the strongest deviations from standard cooling–contraction evolution.

Similarly, Fig. 3 presents the ratio of mass-loss rates with and without ohmic heating for 60–100 M_{\oplus} planets across orbital separations of $a = 0.02$ –0.05 AU. Unlike the monotonic behavior seen in the non-ohmic models of Fig. 2, these ratio plots explicitly isolate the contribution of magnetic dissipation to atmospheric escape. Values above unity mark regimes in which ohmic heating enhances mass-loss rates, while ratios below unity indicate conditions where magnetic energy deposition becomes insufficient to sustain elevated escape.

¹ The magnetic field strengths quoted in this work represent the local dynamo-generated fields within the convective interior, as derived from the scaling relations of Christensen et al. (2009) and Reiners & Christensen (2010). These values should not be directly compared to the surface dipole moments inferred for Solar System planets, which are typically one to two orders of magnitude weaker due to geometric attenuation and field topology.

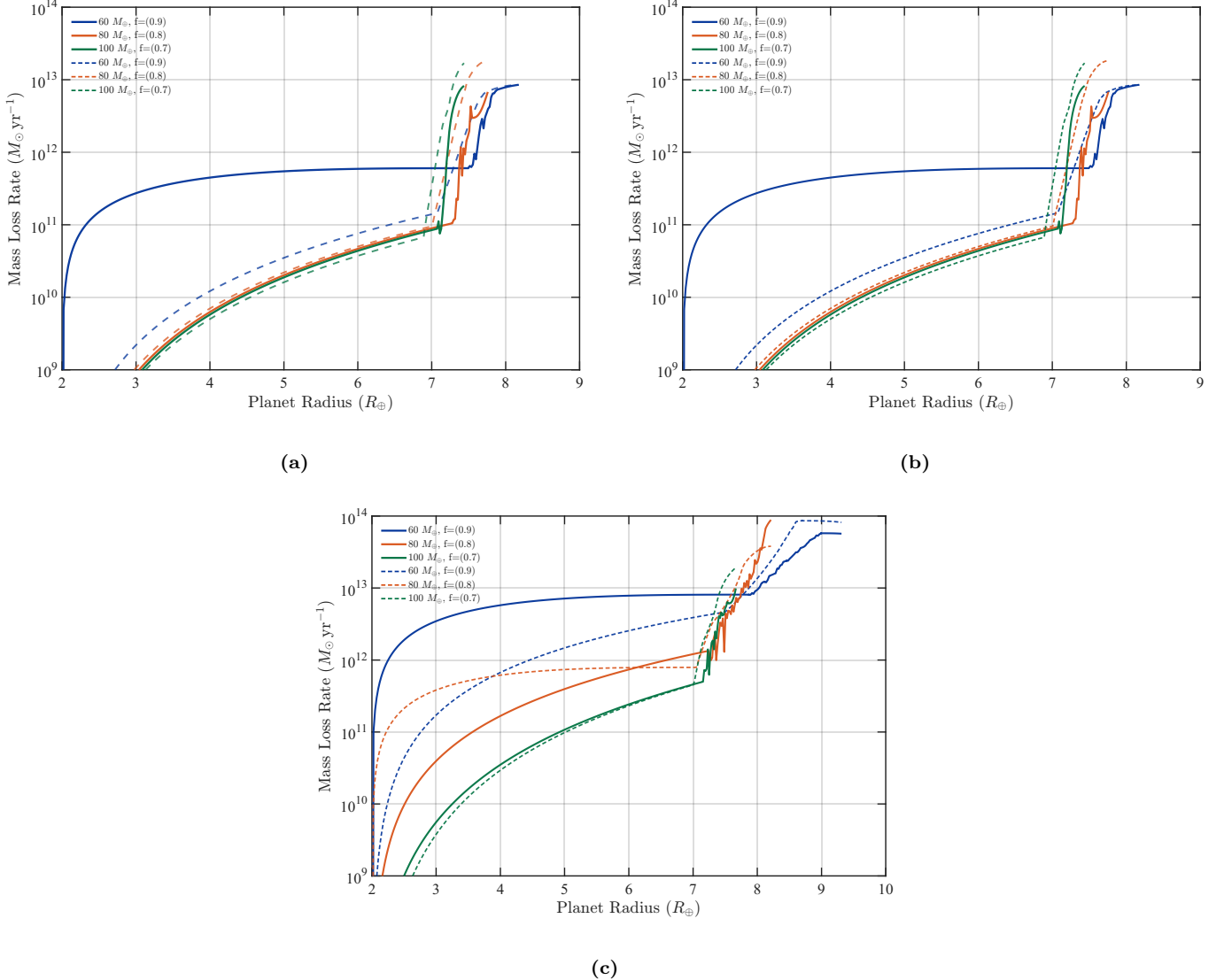


Figure 2: Coupled evolution of radius inflation and atmospheric escape for 60, 80, and 100 M_{\oplus} hot Saturns with (solid) and without (dashed) Ohmic heating. Each panel corresponds to a different orbital separation: (a) — 0.05 AU, (b) — 0.04 AU, and (c) — 0.02 AU. In all close-in cases, magnetic dissipation inflates planetary radii and enhances mass-loss rates by up to one to two orders of magnitude relative to non-Ohmic models, consistent with the exponential inflation mechanism proposed by Pu & Valencia (2017). The persistence of inflated radii even as the planets cool and contract illustrates the self-reinforcing coupling between magnetic dissipation, thermal structure, and hydrodynamic escape, particularly within the sub-Saturn mass regime where Ohmic heating remains energetically significant.

282 Across all three panels—(a) 60 M_{\oplus} , (b) 80 M_{\oplus} , and (c) 100 M_{\oplus} —the enhancement is strongest at small radii
 283 ($R \lesssim 6 R_{\oplus}$), where electrical conductivity and wind–field coupling are highest. In these regions, Ohmic dissipation
 284 boosts escape by up to several orders of magnitude relative to the non-Ohmic baseline. As the planets inflate to larger
 285 radii ($R \gtrsim 6.5\text{--}7 R_{\oplus}$), the ratio declines toward or below unity, reflecting weakened magnetic coupling and reduced
 286 interior current densities. This transition marks the point at which Ohmic heating no longer overcomes the declining
 287 EUV environment or the diminishing conductivity of the envelope.

288 These trends show that ohmic heating introduces a radius-dependent feedback loop: strong coupling at small radii
 289 leads to enhanced escape, which in turn modulates thermal structure and dynamo strength. As the envelope expands,
 290 the feedback weakens and mass-loss rates converge back to their non-ohmic values.

4. DISCUSSION

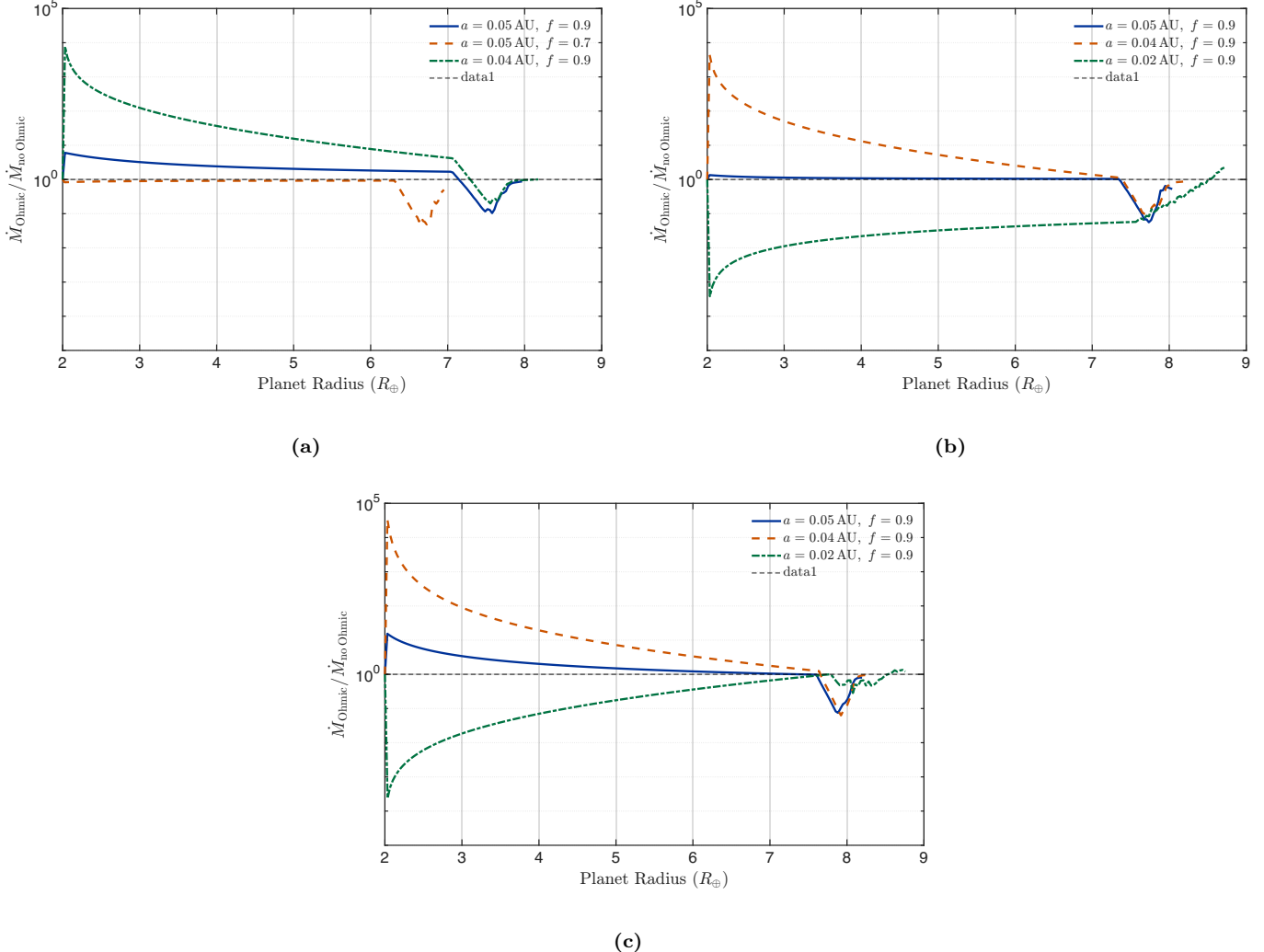


Figure 3: Timseries evolution of planetary radius for a (a) 60, (b) 80, and (c) 100 M_{\oplus} planet masses under several orbital and H/He mass fractions. Each curve corresponds to a different combination of orbital separation (a) and envelope mass fraction (f). Values above unity indicate regimes in which Ohmic heating enhances atmospheric escape, typically at small radii where magnetic coupling and interior conductivity are strongest. At larger radii ($R > 6.5 \sim 7 R_{\oplus}$), certain models fall below unity, reflecting weakened magnetic coupling and reduced Ohmic energy deposition, which suppresses escape relative to the no-Ohmic case. This behavior demonstrates that Ohmic heating can both amplify and regulate mass loss over a planet’s evolution, depending sensitively on envelope thickness and orbital irradiation.

In this study, we have demonstrated that Ohmic heating, when modeled self-consistently with planetary magnetic field evolution, can substantially alter the thermal and mass-loss histories of hot Saturn-mass planets. By linking dynamo scaling with interior luminosity and convective flux, our models capture a time-dependent feedback in which magnetic fields regulate Ohmic dissipation and, in turn, are influenced by the altered thermal structure. We find that lower-mass ($\sim 60 \sim 80 M_{\oplus}$) hot Saturns are particularly susceptible to runaway inflation and hydrodynamic escape, with heating powers exceeding 10^{18} W and late-time mass-loss rates several orders of magnitude above cooling-only predictions. Higher-mass cases ($\sim 100 M_{\oplus}$) remain more resilient, converging toward modest inflation and suppressed escape. These results demonstrate the importance of including magnetic dissipation in evolutionary models of hot gaseous exoplanets.

Our findings build on earlier work that invoked Ohmic heating to explain radius anomalies in hot Jupiters (e.g., Batygin & Stevenson 2010; Wu & Lithwick 2013; Perna et al. 2010) and extended it into the sub-Saturn regime (Pu & Valencia 2017). While prior studies typically prescribed static field strengths, our approach explicitly evolves the dynamo, showing how faster cooling in lower-mass planets produces stronger convective fluxes and initially stronger

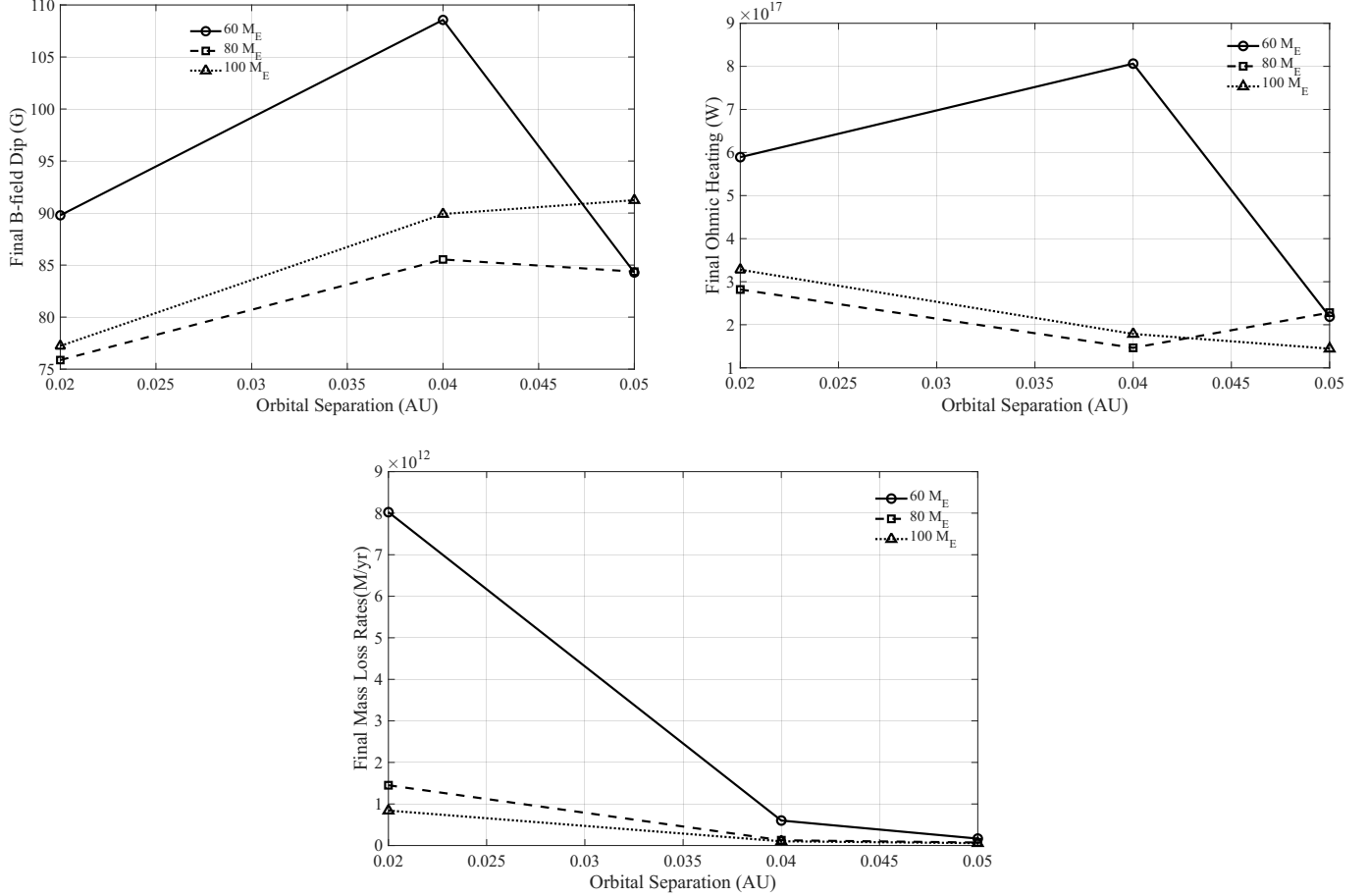


Figure 4: Final planetary properties after coupled evolution with self-consistent magnetic field growth, Ohmic heating, and atmospheric mass loss, shown as a function of orbital separation. From left to right: (a) magnetic dipole strength, (b) radius inflation relative to non-Ohmic models, and (c) late-time mass-loss rates. Different line styles denote planetary masses ($60-100 M_{\oplus}$). The results highlight how lower-mass planets at small separations sustain stronger fields, enhanced Ohmic dissipation, and larger escape rates, whereas higher-mass analogs converge to weaker evolutionary responses.

fields. This helps to explain why Ohmic dissipation can be disproportionately efficient in sub-Saturns, a feature not captured by fixed-field treatments. Our models also align with recent dynamo-scaling predictions (e.g., Christensen et al. 2009; Kilmetis et al. 2024) that suggest a strong mass dependence in field strength, though here we show how this directly translates into divergent thermal and mass-loss pathways.

Recent studies have quantified Ohmic heating produced in upper atmospheres by time-varying external magnetic fields, with applications to small/rocky-to-sub-Neptune planets such as TRAPPIST-1 b and π Men c, and have shown that ionospheric heating can be strong and may even compete with XUV under certain conditions (Strugarek et al. 2025). Here, we model deep-interior Ohmic dissipation driven by winds shearing a planetary magnetic field whose strength co-evolves with the planet’s thermal and convective state. We apply this framework to hot Saturn-mass planets ($60-100 M_{\oplus}$) coupling dynamo scaling to interior evolution and mass loss. In this regime, the interior energy budget and radius evolution dominate the observable outcomes, and we find that Ohmic heating substantially amplifies escape and inflation for lower-mass hot Saturns. The oscillations seen in the Ohmic-heating models (Fig. fig:radius_evolution) are a robust feature of the simulations, persisting across different timestep controls and spatial resolutions. They reflect a self-regulating feedback between magnetic dissipation and convection, where increased Ohmic power temporarily suppresses convective flux until the internal entropy readjusts. This behavior parallels the convective modulation reported by \{vigan2025\}, suggesting that Ohmic heating can drive mild thermal relaxation cycles in hot Saturn interiors.

Our theoretical predictions can be probed with both current and upcoming surveys. Inflated radii persisting into Gyr ages should manifest as outliers in the mass–radius distribution of Saturn-mass exoplanets, a signal accessible to TESS, CHEOPS, and PLATO transit samples. Atmospheric escape enhanced by Ohmic inflation could be detectable via excess Ly α or He 1083 nm absorption, as demonstrated in recent escape detections. Finally, strong magnetic fields implied by our models may be probed indirectly via radio auroral emission or bow-shock asymmetries in transit light curves (Vidotto et al. 2010, 2019; Hess et al. 2014), though such signatures remain observationally challenging. The combination of structural inflation, spectral escape tracers, and magnetospheric diagnostics offers a multi-pronged way to test our framework.

In younger systems, additional effects may modulate Ohmic heating. Gas drag from residual protoplanetary disks could enhance angular momentum loss and regulate the early spin states that influence wind-driven currents. At the same time, elevated accretion luminosities and hotter interiors during the first 100 Myr provide the largest convective fluxes, potentially driving stronger dynamos than at later times. These considerations suggest that Ohmic dissipation may be most dramatic in young, still-cooling sub-Saturns, aligning with the expectation that mass loss is also most vigorous in the early EUV-luminous epoch of the host star. Observations of systems such as GW Ori, with multi-planet gas-rich environments, could provide critical constraints on this early-time coupling.

Although the detailed dependence of magnetic field strength and Ohmic power on orbital separation is non-linear, the combined effect is that lower-mass hot Saturns experience the strongest heating and the highest mass-loss rates, making them the most vulnerable to runaway inflation and atmospheric escape. This instability provides a natural pathway toward explaining the dearth of low-mass close-in Saturns—the so-called “hot-Saturn desert.” By contrast, higher-mass analogs remain buffered against runaway outcomes, helping to explain the population-level asymmetry seen between sub-Saturns and more massive hot Jupiters.

Future work should expand these calculations to account for additional processes and broader parameter ranges. A natural extension is to include tidal dissipation and eccentricity pumping (e.g., Jackson et al. 2016; Louden et al. 2023; Batygin 2025), which may work alongside with Ohmic heating to prolong inflation phases. Exploring a wider range of envelope metallicities and conductivity profiles will further constrain how core composition shapes current penetration and magnetic feedback. Combining improved interior-evolution models (e.g., Tang et al. 2025) with coupled photochemistry and radiative transfer will allow direct comparisons to JWST spectra of warm and hot Saturns.

5. CONCLUSION

Our simulations reveal that Ohmic dissipation, when implemented self-consistently to planetary dynamo evolution, profoundly alters the thermal and mass-loss histories of hot Saturn-mass exoplanets. Lower-mass ($\sim 60 - 80 M_{\oplus}$) planets exhibit runaway inflation and enhanced atmospheric escape, with Ohmic heating powers exceeding 10^{18} W and mass-loss rates up to 1-2 orders of magnitude above standard thermal contraction models without dissipative effects. In this regime, higher-mass ($\sim 100 M_{\oplus}$) analogs in contrast remain comparatively stable, underscoring a strong mass dependence in magnetic–thermal coupling.

In contrast, higher mass $\sim 100 M_{\oplus}$ remain comparatively stable: their radii evolve closer to standard cooling tracks and their mass loss shows modest enhancement. These results demonstrate that magnetic dissipation plays a central role in the coupled thermal and mass-loss evolution of sub-Saturns. Self-consistent treatment of dynamo activity and Ohmic heating reveals a feedback that drives rapid atmospheric erosion in low-mass planets while sustaining inflated radii. Importantly, Ohmic heating cannot be treated as a minor correction to energy balance, but rather as a dominant process shaping the observable radii and escape histories of hot Saturns.

5.1. Data & Code Availability

The data supporting the plots and findings of this study are available from the corresponding author upon request. The most up-to-date version of the code used in this study will be made available upon request and upon publication of the work.

H.C. acknowledges the AI.panther computational facility at Florida Tech, supported by the National Science Foundation MRI Award No. 2016818 (project title: “Acquisition of a High Performance GPU/CPU Cluster for Research and Innovation in Computational Sciences and Engineering”).

REFERENCES

- 369 Batygin, K. 2025, *The Astrophysical Journal*, 985, 87
 370 Batygin, K., & Stevenson, D. J. 2010, *The Astrophysical
 Journal Letters*, 714, L238
 371 Chen, H., & Rogers, L. A. 2016, *The Astrophysical Journal*,
 372 831, 180
 373 Christensen, U. R., Holzwarth, V., & Reiners, A. 2009,
 374 *Nature*, 457, 167
 375 Claire, M. W., Sheets, J., Cohen, M., et al. 2012, *ApJ*, 757,
 376 95
 377 Cohen, M., Palmer, P. I., Paradise, A., Bollasina, M. A., &
 378 Tiranti, P. I. 2024, *The Astronomical Journal*, 167, 97
 380 Connerney, J. E. P., Yelle, R. V., & Waite, J. H. 2018,
 381 *Journal of Geophysical Research: Space Physics*, 123, 27
 382 Freedman, R. S., Lustig-Yaeger, J., Fortney, J. J., et al.
 383 2014, *The Astrophysical Journal Supplement Series*, 214,
 384 doi:10.1088/0067-0049/214/2/25
 385 Ginzburg, S., & Sari, R. 2016, *The Astrophysical Journal*,
 386 819, 116
 387 Gu, P.-G., & Chen, H. 2023, *The Astrophysical Journal
 Letters*, 953, L27
 388 Guillot, T. 2010, *Astronomy and Astrophysics*, 520, A27
 390 Hess, S. L., Echer, E., Zarka, P., Lamy, L., & Delamere, P.
 391 2014, *Planetary and Space Science*, 99, 136
 392 Hess, S. L. G., & Zarka, P. 2011, *Astronomy & Astrophysics*,
 393 531, A29
 394 Hubbard, W. B., Burrows, A., & Lunine, J. I. 2002, *Annual
 Review of Astronomy and Astrophysics*, 40, 103
 396 Jackson, B., Barnes, R., & Greenberg, R. 2008, *The
 Astrophysical Journal*, 681, 1631
 397 Jackson, B., Jensen, E., Peacock, S., Arras, P., & Penev, K.
 398 2016, *Celestial Mechanics and Dynamical Astronomy*,
 399 126, 227
 401 Kilmetis, K., Vidotto, A. A., Allan, A., & Kubyshkina, D.
 402 2024, *Monthly Notices of the Royal Astronomical
 Society*, 535, 3646
 404 Lammer, H., Selsis, F., Ribas, I., et al. 2003, *The
 Astrophysical Journal*, 598, L121
 406 Lopez, E. D., & Fortney, J. J. 2013, *The Astrophysical
 Journal*, 776, 2
 408 Louden, E. M., Laughlin, G. P., & Millholland, S. C. 2023,
 409 *The Astrophysical Journal Letters*, 958, L21
 410 Malsky, I., & Rogers, L. A. 2020, *The Astrophysical
 Journal*, 896, 48
 412 Murray-Clay, R. A., Chiang, E. I., & Murray, N. 2009, *The
 Astrophysical Journal*, 693, 23
 413 Owen, J. E., & Wu, Y. 2013, *The Astrophysical Journal*,
 414 775, 105
 416 —. 2017, *The Astrophysical Journal*, 847, 29
 417 Paxton, B., Bildsten, L., Dotter, A., et al. 2010, *The
 Astrophysical Journal Supplement Series*, 192, 3
 419 Paxton, B., Cantiello, M., Arras, P., et al. 2013, *The
 Astrophysical Journal Supplement Series*, 208, 4
 421 Paxton, B., Marchant, P., Schwab, J., et al. 2015, *The
 Astrophysical Journal Supplement Series*, 220, 15
 423 Perna, R., Heng, K., & Pont, F. 2010, *The Astrophysical
 Journal*, 719, 1421
 425 Pu, B., & Valencia, D. 2017, *The Astrophysical Journal*,
 426 835, 43
 427 Rauscher, E., & Menou, K. 2013, *The Astrophysical
 Journal*, 764, 103
 429 Reiners, A., & Christensen, U. R. 2010, *Astronomy &
 Astrophysics*, 522, A13
 431 Ribas, I., Guinan, E. F., Güdel, M., & Audard, M. 2005,
 432 *ApJ*, 622, 680
 433 Schubert, G., Stevenson, D., & Cassen, P. 1980, *Journal of
 Geophysical Research: Solid Earth*, 85, 2531
 435 Sethi, R., & Millholland, S. C. 2025, *The Astrophysical
 Journal*, 988, 247
 437 Stevenson, D. 1983, *Reports on Progress in Physics*, 46, 555
 438 Storey, P. J., & Hummer, D. G. 1995, *MNRAS*, 272, 41
 439 Strugarek, A., Muñoz, A. G., Brun, A., & Paul, A. 2025,
 440 *Astronomy & Astrophysics*, 693, A220
 441 Tang, Y., Fortney, J. J., Nimmo, F., et al. 2025, *The
 Astrophysical Journal*, 989, 28
 443 Thorngren, D. P., & Fortney, J. J. 2018, *The Astronomical
 Journal*, 155, 214
 445 Tian, F., Toon, O. B., Pavlov, A. A., & De Sterck, H. 2005,
 446 *The Astrophysical Journal*, 621, 1049
 447 Vidotto, A., Feeney, N., & Groh, J. 2019, *Monthly Notices
 of the Royal Astronomical Society*, 488, 633
 449 Vidotto, A. A., Jardine, M., & Helling, C. 2010, *The
 Astrophysical Journal Letters*, 722, L168
 451 Viganò, D., Sengupta, S., Soriano-Guerrero, C., et al. 2025,
 452 *Astronomy & Astrophysics*, 701, A8
 453 Watson, A. J., Donahue, T. M., & Walker, J. C. 1981,
 454 *Icarus*, 48, 150
 455 Wu, Y., & Lithwick, Y. 2013, *The Astrophysical Journal*,
 456 772, 74